ICARUS 53, 262–285 (1983)

Albedo, Internal Heat Flux, and Energy Balance of Saturn[1]

R. A. HANEL, B. J. CONRATH, V. G. KUNDE, J. C. PEARL, AND J. A. PIRRAGLIA

Laboratory for Extraterrestrial Physics, NASA/Goddard Space Flight Center, Greenbelt, Maryland 20771

Received July 9, 1982; October 25, 1982

Full-disk and high-resolution measurements recorded during the Voyager 1 flyby of Saturn by the radiometer of the infrared instrument, IRIS, indicate a geometric albedo of 0.242 ± 0.012, which is lower than previous estimates. The given error is largely due to uncertainties in systematic corrections; random effects are small. Combining this measurement with the Pioneer-derived phase integral yields a Bond albedo of 0.342 ± 0.030. Infrared spectra recorded at the same time by the Michelson interferometer, along with a model extrapolation to wavenumbers not covered by the instrument, yield an effective temperature of 95.0 ± 0.4°K. As in the case of the radiometer, random instrumental errors are small, and the quoted error in the effective temperature reflects primarily uncertainties in systematic corrections. The rings of Saturn significantly affect both the short- and long-wavelength fluxes. From these measurements the internal heat flux of Saturn is 2.01 ± 0.14 10^{-4} W cm^{-2}, and the energy balance, defined as the ratio of total emitted to total absorbed energy, is 1.78 ± 0.09.

1. INTRODUCTION

The determination of the energy balance[2] of Saturn requires accurate measurements of the emitted thermal and absorbed solar energy, with corrections for ring effects. For Jupiter, Voyager measurements yielded an energy balance of 1.67 ± .09 [Hanel *et al.* (1981a); hereafter referred to as Paper 1]. The energy balance of Saturn is more difficult to determine than that of Jupiter because the Saturnian rings have a substantial effect on both the short- and long-wave energy fluxes; in addition, the magnitudes of the emitted thermal and reflected solar radiation are lower at Saturn's heliocentric distance.

Knowledge of the energy balance provides a constraint on models of the planetary interior and evolution (Smoluchowski, 1967; Hubbard, 1968, 1973, 1980, 1981; Hubbard and Smoluchowski, 1973; Graboske *et al.*, 1975; Stevenson and Salpeter, 1976; Cameron and Pollack, 1976; Pollack *et al.*, 1977; Stevenson, 1980). Grossman *et al.* (1980) investigated the evolution of the Saturnian internal heat source from the time of planetary formation to the present and found substantial discrepancies between model and observation, whereas similar calculations for Jupiter show generally good agreement. The energy balances of the Giant Planets are closely linked to their radial helium distributions because separation of helium and hydrogen is believed to be a significant source of internal energy (Smoluchowski, 1967; Salpeter, 1973; Flasar, 1973; Stevenson and Salpeter, 1977). Indeed, Saturn's outer layers have been found to be depleted of helium (Conrath *et al.*, 1982; Hanel *et al.*, 1981b) in contrast to the outer layers of Jupiter (Gautier *et al.*, 1981). Helium differentiation may be substantial in Saturn but is probably not yet significant in Jupiter. Therefore, comparison of the energy balances and the helium abundances of the Giant Planets (as well as their gravitational moments and magnetic properties) is of great interest for under-

[1] Paper presented at the "Saturn Conference," Tucson, Arizona, May 11–15, 1982.

[2] In deference to common usage, we use the term "energy balance," although it is the energy excess or imbalance which is actually evaluated.

0019-1035/83 $3.00
Copyright © 1983 by Academic Press, Inc.
All rights of reproduction in any form reserved.

TABLE I

MEASUREMENTS OF SATURN'S ALBEDO, THERMAL EMISSION, ENERGY BALANCE, AND INTERNAL HEAT

	Bond albedo	Equilibrium temperature (°K)	Effective temperature (°K)	Radiated power/ absorbed power	Internal heat flux (10^{-4} W cm^{-2})
Aumann *et al.* (1969)	$0.45^{+0.12}_{-0.06}$	77^{+2}_{-5}	97 ± 4	$2.5^{+1.3}_{-0.6}$	3
Nolt *et al.* (1974)			99^{+4}_{-3}	$2.8^{+0.6}_{-0.5}$	(3.6)
Rieke (1975)		76 ± 4		2.5 ± 0.6	(2.8)
Wright (1976)	$0.45^{+0.12}_{-0.06}$		85 ± 2	$1.44^{+0.44}_{-0.2}$	(0.9)
Ward (1977)		76 ± 4	89 ± 3	1.9 ± 0.45	(1.7)
Erickson *et al.* (1978)	0.45 ± 0.15	75 ± 5	97 ± 3	2.7 ± 0.8	(3.1)
Courtin *et al.* (1979)			~95	2.4	(2.7)
Gautier and Courtin (1979)		78 ± 3	99.3 ± 4.6	2.6 ± 0.9	(3.4)
Orton and Ingersoll (1980)	0.54 ± 0.15		96.5 ± 2.5	2.8 ± 0.9	3.2 ± 1.0
Melnick *et al.* (1982)	0.337 ± 0.029		96.1 ± 1.6	2.20 ± 0.15	(2.6)
This investigation (1983)	0.342 ± 0.030	82.3 ± 0.9	95.0 ± 0.4	1.78 ± 0.09	2.01 ± 0.14

standing the evolution of these bodies and, by inference, of the primordial solar nebula. So far Jupiter and Saturn have been explored by the Voyager spacecraft; it is planned to explore Uranus and Neptune with Voyager 2 in 1986 and 1989, respectively.

Early measurements by Menzel *et al.* (1926) and later by Low (1966) led to the conclusion that Saturn emits more energy in the infrared than it receives from the Sun; equivalently, the effective temperature, T_{eff}, is larger than the equilibrium temperature, T_{eq}, which the planet would obtain if it were in equilibrium with solar radiation and had no internal heat sources. Recent measurements of Saturn's albedo and thermal emission are summarized in Table I. The Bond albedo, the effective temperature, and the equilibrium temperature which were used by the various authors to derive the energy balance and internal heat flux are shown. Aumann *et al.* (1969) and Orton and Ingersoll (1980) have explicitly evaluated the internal flux. In the remainder of Table I we used stated energy balances and the equilibrium or effective temperatures to determine the internal flux; these values are shown in parentheses. Up to 1977 most investigators used the Bond albedo of 0.45 of Aumann *et al.* (1969); these authors assume the Bond albedos of Saturn and Jupiter to be equal because of the similarity of their spectra between 0.7 and 2.5 μm. The estimate for Jupiter, 0.45, is the value derived by Taylor (1965) using his measurements of the Jovian geometric albedo, 0.28, and an estimate of 1.6 for the phase integral. Tomasko *et al.* (1978) have since shown that 1.25 is a better value for the Jovian phase integral. Erickson *et al.* (1978) based their estimate of Saturn's Bond albedo on an integration of the spectral albedos measured by Walker (1966), Ir-

vine and Lane (1971), and Binder and McCarthy (1973), which resulted in a geometric albedo of 0.36. Combining this with the phase integral of 1.25 of Jupiter, again using a similarity argument, yielded the Bond albedo of 0.45 quoted by Erickson *et al.* (1978). The agreement with the earlier estimate is only coincidental. Orton and Ingersoll (1980) adopted the value of Erickson *et al.* (1978) but corrected for a phase integral of 1.5 that seemed to be in better accord with the preliminary Pioneer data, which became available at that time. The value used by Melnick *et al.* (1982) is taken from a preliminary version of the present work.

Section 2 of this paper discusses the stability of the Voyager radiometer. In Section 3 the geometric albedo of Saturn is determined using the Voyager IRIS radiometer; the Bond albedo is then calculated from the geometric albedo by using the phase integral derived from Pioneer data (M. Tomasko, private communication, 1982). Section 4 presents the corresponding error analysis. The thermal emission of Saturn is derived in Section 5 from infrared spectra recorded by the Voyager interferometer. From the Bond albedo and the thermal emission, the energy balance and the magnitude of the interior heat source are calculated in Section 6; the errors in the interferometer measurements are evaluated in Section 7. The significance of the heat balance measurement is discussed in Section 8. Most of the detailed calculations, especially those concerning corrections for ring effects, have been outlined in appendices.

2. STABILITY OF RADIOMETER CALIBRATION

The instrument has been described by Hanel *et al.* (1980) and the calibration procedures for the radiometer and the interferometer have been discussed in Paper 1. Only one aspect of the radiometer calibration is different here: the time interval between calibration and disk measurement was only a few days for Jupiter, but was 78 days for Saturn. Several diffusor plate calibrations serve to assess the slow degradation of the radiometer with time. Table II summarizes the pertinent data. The DN column shows the difference between diffusor plate and deep space readings expressed in terms of signal digital numbers (DN). The quantity in column 5, the DN times the square of the distance from Voyager to the Sun, should be invariant if degradation has not occurred. The percentage degradation actually found is tabulated in column 6 and the calculated relative response in the last column. In deriving the response, also shown in Fig. 1, we assume that the rate of degradation measured in transit between Jupiter and Saturn, 0.19% per year, applies also to the Earth–Jupiter phase of the mission. The relatively large change at the Jupiter encounter is believed to be due to the effect of high-energy particles on the dichroic mirror which separates the visible and near-infrared from the far-infrared radiation in IRIS (Hanel *et al.*, 1980). Micrometeorite erosion of the highly reflective and fully exposed primary mirror of the IRIS telescope may also contribute

TABLE II

RADIOMETER CALIBRATION MEASUREMENTS IN SPACE

Time	Date	DN	$(AU)^2$	DN/$(AU)^2$	Δ (%)	Resp (%)
Before Jupiter	7 Feb 79	1151	26.2886	30258.18		99.71
After Jupiter	11 Apr 79	1022	29.3341	29979.45	0.921	98.79
Before Saturn	6 Aug 80	400	74.7484	29899.35	0.267	98.53
After Saturn	13 Jan 81	310	96.1606	29809.78	0.300	98.23

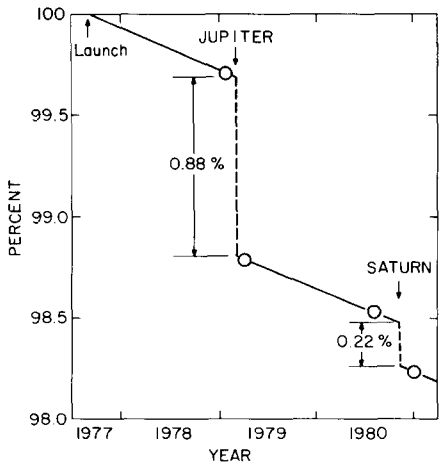

FIG. 1. The degradation of the radiometer sensitivity with time. Straight line segments are fitted to the four diffusor plate calibrations, which were made before and after each planetary encounter.

to the more gradual degradation and the small effect near Saturn. The degradation shown in Table II and Fig. 1 is the product of changes in the radiometer *and* the diffusor plate; we have no direct way of separating the effects; but it seems more likely that most of the degradation is in the more complex radiometer rather than in the bead-blasted surface of the diffusor plate. In this analysis we assume that the diffusor plate did not change, but in the error analysis discussed below we allow for the extreme case in which all of the observed change is attributed to the plate and none to the radiometer. In either case the combined degradation of the radiometer, the highly reflective 50-cm telescope, and the diffusor plate was less than 2% after more than 3 years of flight through the solar system.

The spectral bandpass of the IRIS radiometer extends from 0.3 to 1.8 μm; the remainder of the solar spectrum is accounted for by adjusting the measured intensities using ground-based determinations of the relative spectral characteristics of the planet and the diffusor plate mounted on the spacecraft (see Paper 1).

3. THE GEOMETRIC AND BOND ALBEDOS

Because of Saturn's long radiative time constant, the value of the absorbed solar energy, which is relevant to the energy balance, is the average over one Saturnian year. However, the observations were acquired at a single time in the seasonal cycle, that is, for one particular ring illumination angle. We therefore first use the radiometer measurements to determine the geometric albedo which would be obtained in the complete absence of the ring system. This result is multiplied by the phase integral obtained from Pioneer to arrive at the Bond albedo. The total annual mean energy absorbed by the atmosphere is then calculated, taking into account the seasonal variation of the additional energy scattered and emitted by the rings onto the planet and of the energy prevented from reaching the planet by ring shadowing.

The full-disk measurements for our analysis were made just before the apparent equatorial diameter of Saturn equalled the angular diameter of the instrument's field of view, requiring adjustments for the differences in solid angle, Saturn's oblateness, and nonuniformity of the instrument's response within the field of view. All full-disk data used in this analysis were recorded between 4 and 13 hr after turn-on when Saturn's equatorial diameter grew from 0.967 to 0.982 of the IRIS field of view. During these critical hours IRIS was pointed at Saturn, sometimes well centered on the planet, sometimes slowly drifting off. Maxima of the radiometer readings and of the infrared spectra obtained by the interferometer were selected. Out of these temporal maxima a subset of eight measurements was chosen for which it can be safely assumed that the disk of Saturn was entirely within the field of view. A perfectly aligned IRIS field of view is shown in Fig. 2 superimposed on a Saturnian image taken by Voyager 1. To obtain the geometric albedo from the data requires the introduction of corrections which account for obscuration

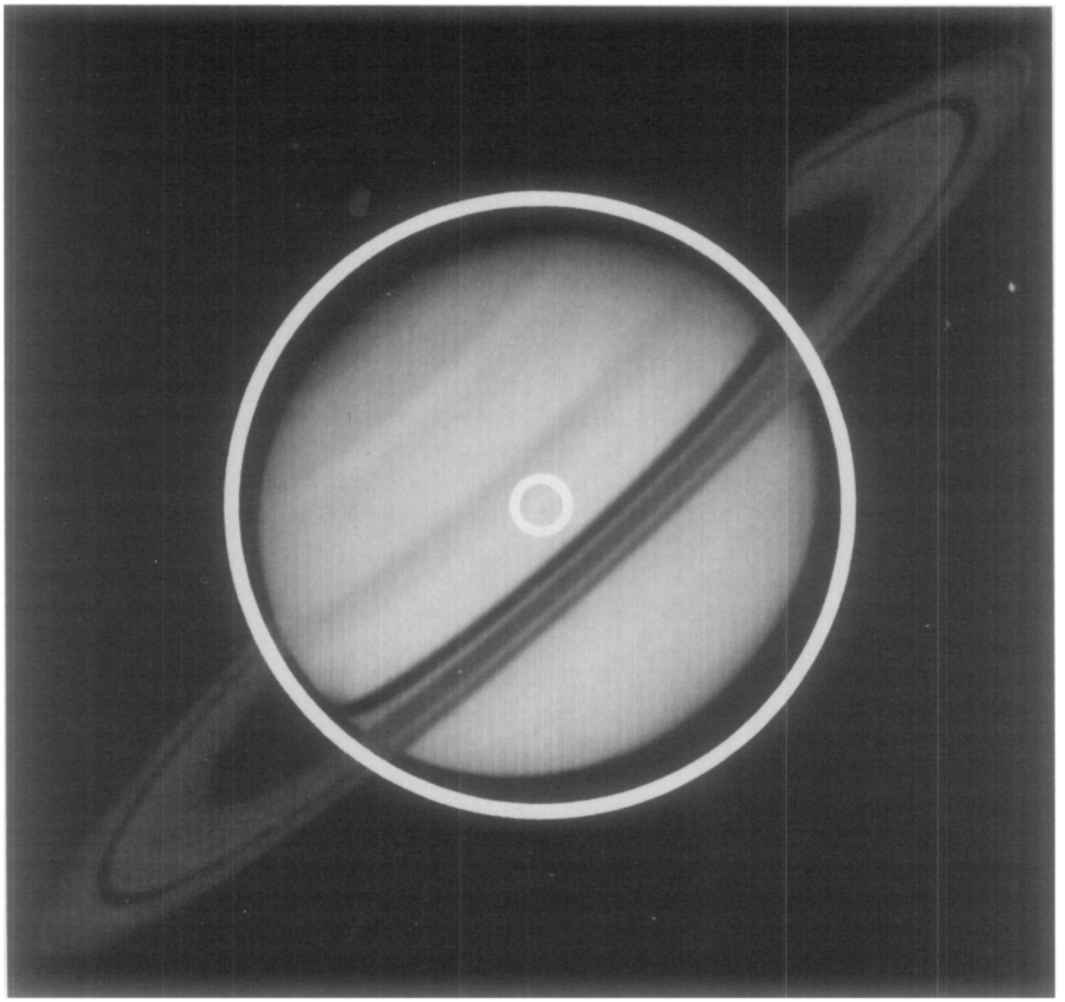

FIG. 2. This image of Saturn was taken by the Voyager 1 narrow-angle camera at approximately the time of the full-disk measurements by IRIS. During the series of disk observations, the apparent IRIS field of view decreased by an amount indicated by the annular width of the superimposed large circle. The small circle represents the size of the field of view during the north–south mapping observations.

and shadowing of the planet by the rings, and for reflection and scattering of sunlight directly and indirectly via Saturn from the rings into the radiometer. A further correction is required to account for the nonzero phase angle of the measurements. The corrected radiometer signal is then used with calibration measurements from an on-board diffusor plate to obtain the geometric albedo of Saturn.

Several adjustments are made to the individual radiometer readings in order to reduce them to an equivalent common geometry; the additional adjustments are then made to a weighted average of these results. A block diagram of the steps necessary to determine the absorbed power from the radiometer data is shown in Fig. 3; the numerical results are summarized in Table III.

The first of the corrections applied to each of the radiometer readings concerns sunlight reflected to the instrument from the fraction of the rings within the field of

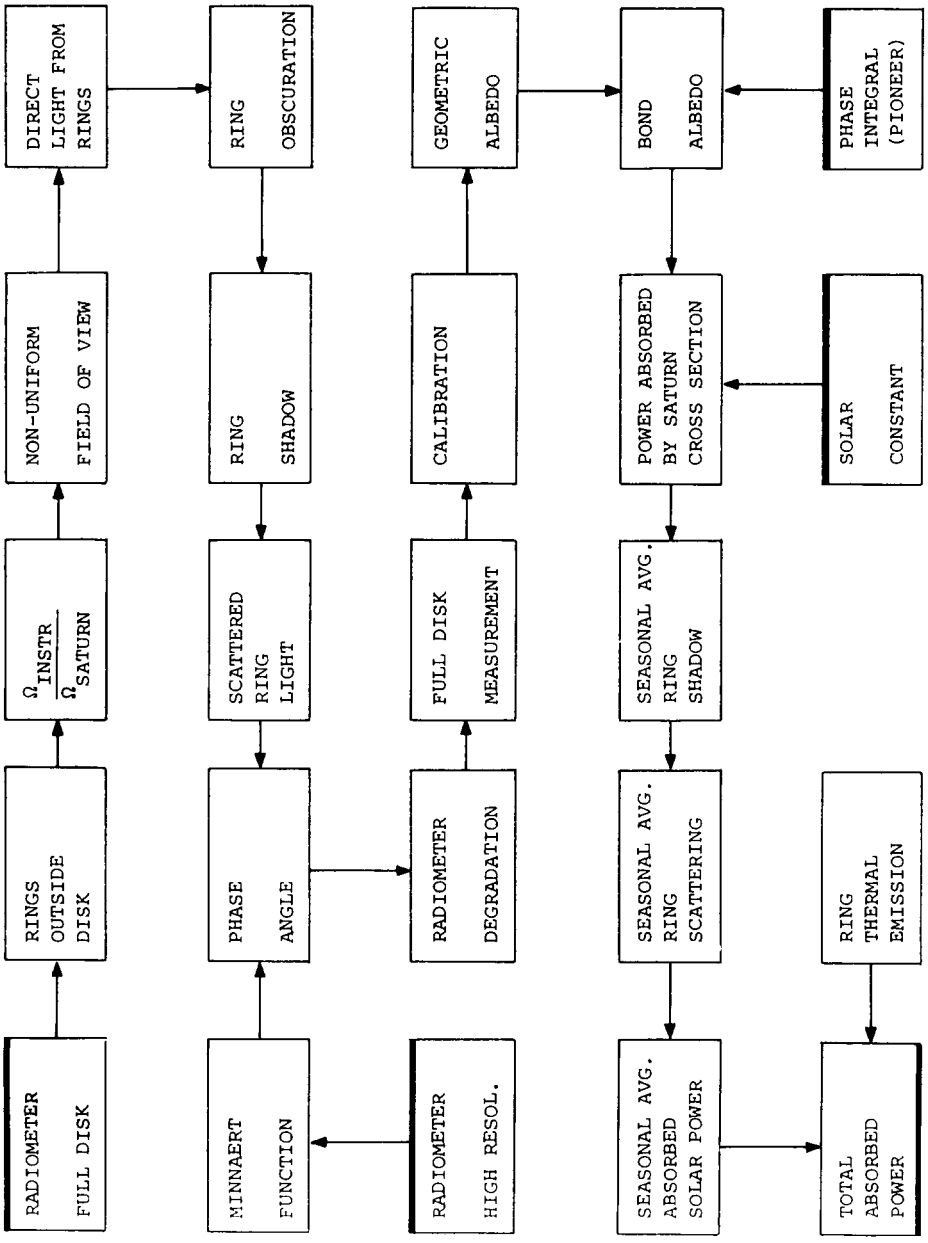

FIG. 3. Block diagram for analysis of the radiometer data. The steps involved in deriving the seasonal average of the solar power absorbed by Saturn are shown. A heavy bar above a block indicates a measurement or another input; the heavy bar below the last block indicates the result.

TABLE III

SUMMARY OF RADIOMETER MEASUREMENTS AND ERRORS

Quantity	Value	Uncertainty	Contributing error (%)
$RD_k = (RD_{0k} - r_{1k})r_{2k}/(1 + r_{3k})$			
RD_{0k}: Disk radiometer measurements	177.6–182.6 DN	3 DN	1.79
r_{1k}: Off-disk ring extension	0.9–0.6 DN	20%	0.09
r_{2k}: Field of view normalization	1.181–1.147	1%	1.07
r_{3k}: Nonuniform field correction	0.025–0.021	20%	0.49
RD_k: Adjusted radiometer measurements	202.2–206.3 DN	4.1 DN	2.14
$RD = (\langle RD_k \rangle + 1\sigma - r_4)(1 - r_7)/(1 - r_5)(1 - r_6)(1 - r_8)(1 - r_9)$			
$\langle RD_k \rangle$: Raw disk average	204.0 DN	1.5 DN	0.77
r_4: Light reflected from rings	14.8 DN	10%	0.77
r_5: Disk obscuration by rings	0.0879	10%	0.96
r_6: Ring shadow on disk	0.0459	10%	0.48
r_7: Ring light scattered to disk	0.0124	20%	0.25
r_8: Phase function	0.0228	0.6%	—
r_9: Radiometer degradation	0.0004	—	—
RD: Adjusted disk average	221.7 DN	5.9 DN	2.64
$P_{Sat} = P_{Diff} \frac{RD}{R_{Diff}} \left(\frac{AU_{Sat}}{AU_{Diff}}\right)^2 \left(\frac{\bar{\tau}_{Diff}}{\bar{\tau}_{Sat}}\right) \cos \beta_{Diff}$			
P_{Diff}: Reflectivity of diffusor plate	0.502	0.018	3.60
RD: Adjusted disk average	221.7 DN	5.9 DN	2.64
R_{Diff}: Diffusor plate radiometer signal	400 DN	3 DN	0.75
$(AU_{Sat}/AU_{Diff})^2$: Distance normalization	1.210	—	—
$(\bar{\tau}_{Diff}/\bar{\tau}_{Sat})$: Integrated spectral transmittance	0.829	0.017	2.00
$\cos \beta_{Diff}$: Orientation of diffusor plate	0.866	0.004	0.50
P_{Sat}: Geometric albedo	0.242	0.012	4.98
q_{Sat}: Phase integral	1.42	0.1	7.1
A_{Sat}: Bond albedo of Saturn	0.342	0.030	8.6

view but off the apparent disk of Saturn. In calculating this ring contribution, and in most subsequent calculations of ring effects, the A, B, and C rings are treated as thin, homogeneous annuli of optical thickness of 0.4, 1.2, and 0.09 with outer and inner radii of 2.26 and 2.01, 1.95 and 1.53, and 1.53 and 1.21 Saturn radii, respectively (Cuzzi, 1978; Smith *et al.*, 1981; Hanel *et al.*, 1982). At the time of the full-disk observations, Voyager was 8.825° above the ring plane. Numerical calculations (see Appendix A), yield ring contributions ranging from 0.75 to 0.47% for the selected set of data. Measurements at closer range of the left and right ansae of Saturn's A and B rings yielded an average radiometer signal of 168 DN. Adopting this value and noting that one out of the four ring segments is in Saturn's shadow due to the 12.65° phase angle (see Fig. 2), the corrections applied to each radiometer reading range from 0.94 to 0.59 DN.

A second, more substantial correction accounts for the fraction of the field of view filled by the apparent disk of Saturn. Each datum was multiplied by the ratio of solid angle of the instrument field of view and the solid angle of Saturn at the time of measurement. In these computations the equatorial

radius of Saturn was assumed to be 60,330 km and the polar radius 54,538 km (Kliore *et al.*, 1980). The ratios of the solid angles range from 1.181 for the earliest to 1.147 for the latest of the data considered.

The third correction applied to each of the radiometer data accounts for the small nonuniformity of the radiometer response within the field. This nonuniformity is apparent in Fig. 1 of Paper 1. We use the relationship between response and fraction of field of view established during the Jupiter encounter to correct for this effect at Saturn. The late instrument turn-on prevented a corresponding long series of observations before Saturn filled the field. The DN value of each reading was divided by the factor

$$1 + 0.1652 \frac{\Omega_i - \omega_s}{\Omega_i} \qquad (1)$$

(where ω_s and Ω_i are the solid angles of Saturn and the instrument field of view, respectively) to obtain the value which would have been obtained if Saturn's image were uniformly distributed over the radiometer's field. These factors range from 1.025 to 1.021.

With the above corrections all radiometer values should be the same if pointing were perfect in all cases. Indeed, the weighted average of all eight data points is 203.99 DN with a standard deviation of 1.47 DN, corresponding to a probable error of 0.72%. The construction of an envelope to the data, as in Fig. 1 of Paper 1, was not possible because the observations were not spread over a long temporal baseline. However, if we assume that the scatter in a similar sequence of Saturn data would be the same as the scatter observed at Jupiter, then comparison with Fig. 1 of Paper 1 suggests that a best estimate for the restricted Saturn data set will be obtained by adding 1σ to the average. To take advantage of the full data set available, we therefore adopt the weighted average plus the 1σ value of the standard deviation to represent the radiometer reading for good alignment with Saturn (205.46 DN), instead of simply choosing the maximum radiometer reading (206.32 DN). The remaining corrections, discussed below, are applied to this weighted mean value.

Correction 4 accounts for sunlight reflected by the rings directly into the instrument field. The rings were found to occupy 8.79% of Saturn's disk (see Appendix B). Again assuming that the ansae measurements of 168 DN are representative, the contributions of the rings in front of the disk to the measured signal amount to 14.76 DN. In addition to reflecting light directly into the field, the rings also obscure some of the illuminated part of the disk. The obscuration is also 8.79% as discussed in Appendix B; this requires that the radiometer value be increased by 18.38 DN. Furthermore, the rings cast a shadow onto Saturn. With the same calculations used to determine the ring obscuration, but using the Sun angle above the ring plane (3.867°) instead of the elevation of the spacecraft above the ring plane (8.825°), the fraction of Saturn's disk in the shadow was found to be 4.59%, requiring a correction of +10.06 DN. A small overlap of the rings with their shadow, mostly in the C ring, has been ignored.

The seventh correction accounts for sunlight scattered by the rings onto the disk of Saturn. This correction, about 1.2%, is more difficult to obtain (see Appendix C). The computations assume that the rings scatter with a phase function appropriate to a large number of Lambert spheres, isolated from each other in space, but fully illuminated by direct and by indirect sunlight reflected from Saturn. For this particular correction the planet is also assumed to scatter sunlight according to the Lambert law. The uncertainty due to the yet unknown phase function of the rings is much larger than the error due to the assumption of a Lambert behavior of Saturn; since this correction is small the latter assumption is considered adequate in this case. The calculations were carried out over the northern hemisphere, using the orbital position

of Saturn at the time of observation (S = 8.31° from the equinoxes). Only light scattered by the C ring was considered to illuminate both hemispheres. The weighted mean contribution of light reflected from the rings (reflectivity 0.6) and doubly reflected from the disk of Saturn (reflectivity 0.342) was determined. This contribution requires subtraction of 2.72 DN from the radiometer value.

The eighth adjustment to the radiometer value accounts for the nonzero phase angle at the time of observation. To determine the phase function, high spatial resolution data were employed. Such data do not require corrections for the field of view or the uniformity of the instrument response; only the local reflective properties of Saturn and their uniformity over the globe must be considered. Among the limited number of data available, we chose two sets in the southern hemisphere, for which the resolution was $\frac{1}{13}$ of the disk diameter or better. Phase angles were between 16 and 34°, and the latitudes of the observations were between −11 and −32°, within a region showing little contrast in the visible (Smith *et al.*, 1981).

The Minnaert function has previously been used to describe limb darkening on Jupiter and Saturn (Binder and McCarthy, 1973). The intensity, I, from a unit surface area is assumed to obey the relation $\log(I\mu) = k \log(\mu\ \mu_0) + \log I_0$, where I_0 is the intensity at normal viewing and illumination, and μ and μ_0 are the cosines of the emission and illumination angles, respectively. The slope k characterizes the local scattering properties: for a Lambert diffusor $k = 1$; for a uniform disk (no limb darkening) $k = 0.5$. Both I_0 and k are generally functions of phase angle and wavelength. The two sets of IRIS radiometer data are plotted in Fig. 4. The linear behavior indicates both that the Minnaert representation provides a reasonable limb function and that the sensitivity of the parameters k and I_0 to phase angles in the range 16–34° is small. Fitting the data yields $k = 0.90$; we assume that this is also appropriate for angles less than 16°.

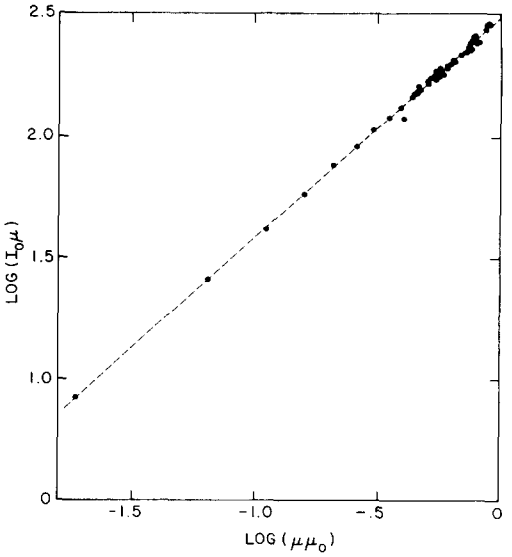

FIG. 4. Minnaert diagram for high-resolution IRIS radiometer observations. Data were recorded for phase angles between 16 and 34° at spatial resolutions between $\frac{1}{13}$ and $\frac{1}{33}$ of the disk diameter. All observations were made at latitudes between −11 and −32°.

Viewed from within the equatorial plane, the functional behavior of the phase function of a Minnaert ellipsoid of revolution under equinoctial illumination is identical to that for a Minnaert sphere. During the observation, the spacecraft was nearly in the equatorial plane, and Saturn had just passed the northern spring equinox. A multiplicative factor of 1/0.9772 then corrects for the observed phase angle ϕ_0 = 12.65°, giving an increase of 5.04 DN (Appendix D).

Finally, with a degradation rate of 0.19% per year and 78 days (6 Aug.–23 Oct.) between calibration and Saturn disk measurements, the ninth correction (for radiometer degradation) is −0.04%, leading to a final value for the disk measurement of 221.71 DN. This is the radiometer signal which would have been measured at zero phase angle, with Saturn filling the IRIS field perfectly, and with the rings completely absent. Somewhat less representative estimates based on high-resolution data alone are consistent with this value (Appendix E).

4. THE GEOMETRIC AND BOND ALBEDOS

The radiometer signal for the disk is converted to the geometric albedo by using the relation

$$\frac{DN_{Sat}}{DN_{Diff}} = \frac{(AU_{Diff})^2 \bar{\tau}_{Sat} p_{Sat}}{(AU_{Sat})^2 \bar{\tau}_{Diff} p_{Diff} \cos \beta_{Diff}}, \quad (2)$$

which is identical to Eq. (5) of Paper 1 except that the phase function is already included in the DN value for the disk measurement of Saturn. The signal from the diffusor plate calibration is 400 DN. The distance between the Sun and spacecraft at the time of radiometer calibration (6 Aug. 1980) was 8.645 AU and the distance between the Sun and Saturn at the time of the planetary disk measurement (23 Oct. 1980) was 9.509 AU. The weighted transmittances of the radiometer for Saturn, $\bar{\tau}_{Sat}$, and the diffusor plate, $\bar{\tau}_{Diff}$, are 0.1783 and 0.1478, respectively. In this calculation, (see Paper 1 for details) the relative spectral characteristic of Saturn between 1.0 and 2.5 μm is taken from Fink and Larson (1979) and between 0.58 and 1.1 μm with an extrapolation down to 0.3 μm from unpublished data of Cruikshank and Hardorp (1981). It should be emphasized that the ground-based measurements provide only the spectral shape while the diffusor plate measurements provide the absolute calibration. The geometric albedo of the diffusor plate, p_{Diff}, is assumed to be 0.5018, the value determined before launch. For all diffusor plate calibrations the angle β between the Sun and the normal to the plate was 30°. With these numerical values the geometric albedo of Saturn, p_{Sat}, is found to be 0.242.

The IRIS data are presently inadequate to determine the phase integral. Additional high-resolution observations (made near the phase angles of 55, 80, and 135°) appear to suffer from substantial pointing uncertainties; without adequate information over a wide range of phase angles, the global scattering properties of Saturn cannot be evaluated. Although the Minnaert limb function derived above can be integrated over the globe (assuming I_0 and k to be constant) to provide an analytic relation for the phase integral, the usefulness of such a calculation would be questionable. Not only does this result fail to conserve energy when I_0 corresponds to unit reflectivity at the subsolar point, but Saturn shows significant variation in the parameters I_0 and k for large phase angles (M. Tomasko, private communication, 1982).

Using Pioneer data to phase angles of 150°, together with a double Henyey–Greenstein single particle scattering function, Tomasko and co-workers (M. Tomasko, private communication, 1982) have determined the phase integral of Saturn for two different models at blue and red wavelength. For a "zone" model, they find q = 1.43 and 1.41 in the blue and red channels, respectively; for a "belt" model, the corresponding values are 1.45 and 1.41. The red channel is near the peak of the reflected spectrum of Saturn (see Fig. 8). We estimate the bolometric phase integral by averaging the Pioneer results, giving triple weight to the red; this yields q = 1.42. Combining this with the estimate of the geometric albedo, we obtain a value of 0.342 for the Bond albedo of Saturn.

Because Saturn is nonspherical, its scattering properties are not independent of the subsolar latitude. For a Minnaert ellipsoid with k = 0.9 and Saturn's ellipticity and obliquity, both the geometric albedo and the phase integral vary about 2% over a season; however, because of opposite senses of these changes, the corresponding variation in the Bond albedo is less than 0.3%, with a seasonally averaged increase over the equinoctial value of approximately 0.1%. We neglect this slight correction.

5. ERROR ANALYSIS FOR GEOMETRIC AND BOND ALBEDOS

The random error in the radiometer measurement is relatively small, but systematic errors which are difficult to specify quantitatively are undoubtedly present. We estimated the various uncertainties and, to ob-

tain an overall measure of the accuracy of our results, treated all of them as uncorrelated standard errors. The relationships between the various quantities, the values and uncertainties of the quantities, and the equivalent percentage contribution of the uncertainty for the overall error estimate are given in Table III.

Contributing errors arising from the individual measurements and their adjustments (top section of Table III) are evaluated relative to the means of the various quantities. The 3 DN uncertainty in a measurement is much larger than the random error, and mainly represents a very conservative estimate of the baseline drift. Relative to the mean value of the measurements, this contributes a 1.79% uncertainty to the final adjusted disk average. Although the estimated uncertainty in the calculations of the ansae measurements for the off-disk extension of the rings is large (20%) the net effect on the overall radiometer result is negligible (0.09%) because the correction itself is small. The error in the field of view factor is assumed to be only 1% because the solid angles of Saturn at the time of measurement and of the instrument are well known. The effect of the nonuniformity of the field has been assigned an uncertainty of 20%. The overall 2.14% contributing error from the adjusted radiometer measurements reflects the associated random and systematic uncertainties from the individual measurements.

The standard deviation of the raw disk average (1.47 DN) is considered as an additional random uncertainty in the error analysis. The uncertainties of 10% in the calculations of the reflected light, the obscuration, and the shadow effects are smaller than the uncertainties in other corrections, since they are related primarily to geometric factors. The term representing scattered light from the rings onto Saturn has been assigned an uncertainty of 20% because of uncertainties in the phase function of the rings. Uncertainty in the phase function of Saturn arises primarily from uncertainty in the limb darkening coefficient, k. By using spectrophotometric data at lower spatial resolution, Binder and McCarthy (1973) have found k values between 0.7 and 1.1; variations are found both with wavelength and in comparing values derived from the north–south and from the east–west scans. We assume that our broadband, high spatial resolution measurements will show lower variability, and assign an uncertainty of 0.1 to our value of k. Assuming the Minnaert formalism to be valid over our range of phase angles ($<34°$), this yields an uncertainty of less than 0.6% in the correction to zero phase. Assuming statistical independence of the errors in the individual corrections, a total probable error of 2.64% is obtained; the full-disk measurement is then 221.7 ± 5.9 DN.

The uncertainties associated with the diffusor plate are assumed to be the same as in Paper 1 except for a possible 1.8% change in plate reflectivity in space which is taken equal to the combined degradation of diffusor plate reflectivity and radiometer response observed over 3 years; together, these lead to a 3.6% uncertainty in the plate reflectivity. The resulting standard error for the geometric albedo is 5.0%. M. Tomasko (private communication, 1982) has estimated an uncertainty of 0.05 in the values of the phase integral derived from the Pioneer data. Additional uncertainty arises from our use of a weighted average of Pioneer results to estimate the overall bolometric phase integral; as we have no objective way of determining this we arbitrarily assign double the uncertainty given by Tomasko to our weighted value. Together these lead to a total 8.6% uncertainty in the Bond albedo.

6. THERMAL EMISSION

Calibrated thermal spectra are used to establish the thermal emission of Saturn. Within the spectral range of the instrument, the spectrum is integrated directly; thermal profiles derived from these same data are used with known opacity sources to deter-

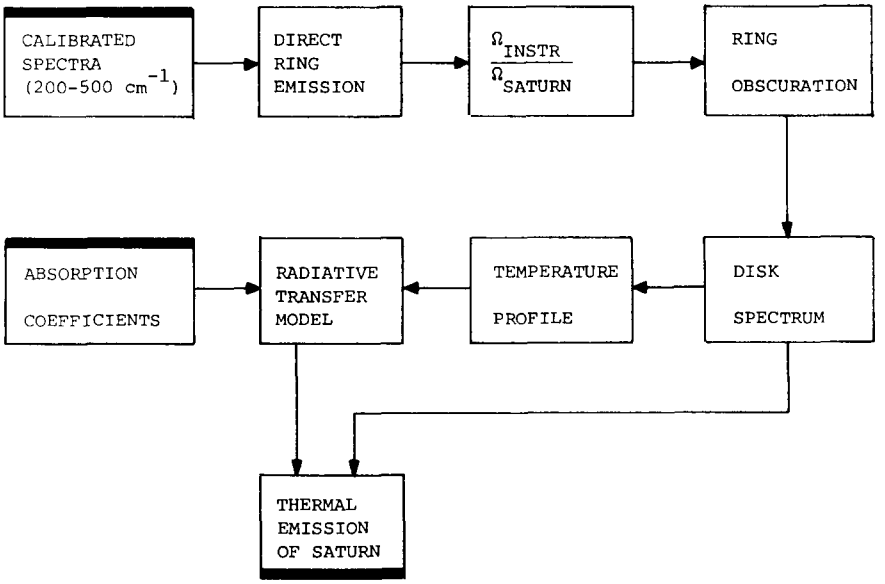

FIG. 5. Block diagram for analysis of the interferometer data. The bars above and below the blocks have the same meaning as in Fig. 3. The direct contribution from the disk spectrum to the total thermal emission is for the 200- to 500-cm^{-1} interval. The radiative transfer model is used to provide estimates of the thermal emission below and above this spectral interval.

mine the emission at other wavelengths. The methodology is summarized in the block diagram of Fig. 5; numerical results are given in Table IV.

Two groups of data are used in the determination. Disk measurements obtained simultaneously with the first set of radiometer data measure the global average flux directly. Alternatively, numerous data from a north–south mapping sequence obtained near closest approach to Saturn are averaged to provide an independent estimate of the global flux.

In treating the disk measurements, each of the eight spectra was multiplied by the ratio of the solid angle of the IRIS field of view to that of Saturn at the time of measurement; thermal emission from the rings which are within the field of view and obscuration of the surface of Saturn by the rings were taken into account. In calculating the thermal emission from the rings at the time of the observations, we assume the A, B, and C rings to be at temperatures of 69, 68, and 85°K, respectively (Hanel *et al.*, 1982); to occupy the fractions of the field and the disk, as discussed in the treatment of the radiometer data; and to radiate with a wavelength-independent emissivity of unity. The ring temperatures were measured by Voyager 2, 9 months after Voyager 1 encounter with Saturn. At the Voyager 1 encounter, the rings were slightly cooler, but we neglect this difference. As in the radiometer analysis a factor correcting for the nonuniformity of the response across the field of view was applied. This factor was derived from the Saturn measurements discussed above and from measurements taken when the diameter of the field of view of the interferometer was about equal to the polar diameter of Saturn. This correction requires a reduction of the measured full-disk radiance by a factor of 0.9766. The resulting average Saturn spectrum is shown in Fig. 6. We integrated each of the selected spectra from 200 to 500 cm^{-1} and found the average integral to be 7.274 10^{-5} W cm^{-2} sr^{-1} with a standard deviation of 0.139 10^{-5} W cm^{-2} sr^{-1}. As in the case of

TABLE IV

SUMMARY OF THERMAL EMISSION MEASUREMENTS AND ERRORS

Quantity	Value	Uncertainty	Contributing error (%)
$ID_k = ID_{0k} r_{2k}$			
ID_{0k}: Disk integral (200–500 cm^{-1}), 10^{-4} W cm^{-2} sr^{-1}	0.578–0.607	—	
r_{2k}: Field of view normalization	1.181–1.147	1%	
ID_k: Adjusted disk integral, 10^{-4} W cm^{-2} sr^{-1}	0.682–0.703	1.03%	
$ID = (\langle ID_k \rangle + 1\sigma - i_1)/(1 + i_2)(1 - i_3)$			
$\langle ID_k \rangle$: Raw disk average, 10^{-4} W cm^{-2} sr^{-1}	0.6902	0.0071	1.05
i_1: Ring emission, 10^{-4} W cm^{-2} sr^{-1}	0.0180	20%	0.53
i_2: Nonuniform field correction	0.0240	20%	0.47
i_3: Disk obscuration by rings	0.0879	10%	0.96
ID: Adjusted disk average (200–500 cm^{-1}), 10^{-4} W cm^{-2} sr^{-1}	0.727	0.014	1.90
IM: Average (200–500 cm^{-1}) using temperature profile from north–south mapping data, 10^{-4} W cm^{-2} sr^{-1}	0.714	0.010	1.40
Weighted mean emission (200–500 cm^{-1}), 10^{-4} W cm^{-2} sr^{-1}	0.719	0.008	0.6
Model emission outside of 200–500 cm^{-1}, 10^{-4} W cm^{-2} sr^{-1}	0.750	3%	1.5
Total thermal radiance, 10^{-4} W cm^{-2} sr^{-1}	1.469	0.024	1.6
T_{eff}: Effective temperature, °K	95.0	0.4	

the radiometer measurements we took the mean value of the spectral radiances and added 1σ to represent the disk measurement for good alignment with Saturn. From the adjusted disk average spectrum we derive a temperature profile assuming an effective emission angle of 48°, as was done for Jupiter in Paper 1; the H_2 and He mole fractions are assumed to be 0.94 and 0.06, respectively (Hanel *et al.*, 1981b). The resulting profile is the warmer of the two shown in Fig. 7.

In using data from the north–south mapping sequence, vertical temperature profiles for different latitudes are derived from longitudinally averaged spectra. Weighting these profiles by area yields the planetary average profile shown in Fig. 7. The disk profile is about 0.3°K warmer than the planetary average profile near 300 mbar, where the atmospheric temperature equals the effective temperature. This method of analysis does not require adjustments for the difference in solid angles between instrument and Saturn, the rings, or the uniformity of the instrument response within the field of view. By using a radiative transfer model and known opacity sources (see below) a disk spectrum is generated from this profile. Integrating from 200 to 500 cm^{-1} yields a radiance of 7.143×10^{-5} W cm^{-2} sr^{-1}, with an estimated uncertainty of 1.4%. The mean of the disk and mapping results, weighted inversely as the square of their estimated errors, is then 7.189×10^{-5} W cm^{-2} sr^{-1}.

The next step in the analysis is to extrapolate the weighted mean spectrum below

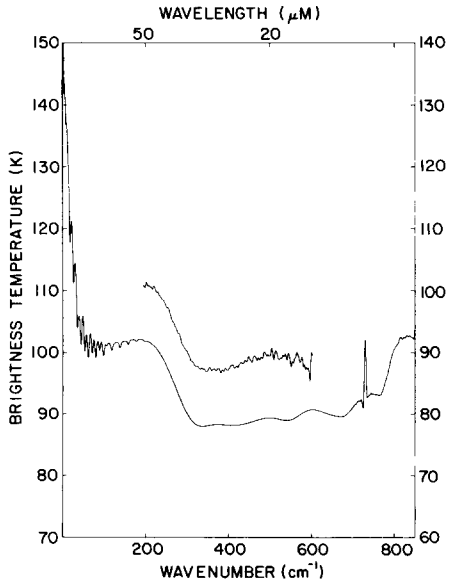

FIG. 6. Upper curve: temperature scale on the right. Average of eight individual disk spectra. Corrections for differences in the field of view and for emission and obscuration by the rings have been applied. Lower curve: temperature scale on the left. Disk spectrum calculated by a radiative transfer model using the temperature profiles derived from the average spectrum and the north–south mapping sequence. Differences in radiance resulting from the imperfect fit between 350 and 600 cm^{-1} are small, and are accounted for in the error analysis.

200 cm^{-1} and above 500 cm^{-1}. Below 200 cm^{-1} the interferometer is insensitive and above 500 cm^{-1} the signal-to-noise ratio of the average of only eight individual spectra is small. The radiative transfer program used for the extrapolation accepts the temperatures derived from the average profile; we extended the temperature profile to higher altitudes using the profile derived from a very large average of data taken during the mapping sequence. Below the 700-mbar level the profile was extended adiabatically. The atmospheric opacity used in the radiative transfer program includes absorption by the pressure-induced hydrogen lines, and by PH_3, NH_3, C_2H_2, and C_2H_6 transitions. The H_2 and He abundances were identical to those used in the temperature analysis. The NH_3 mole fraction was assumed to be the solar value of 1.78×10^{-4} (Lambert, 1978) for the well-mixed region, and to follow the saturation law in the upper troposphere. The PH_3, C_2H_2, and C_2H_6 abundances were adopted from Courtin *et al.* (1981). The calculated spectrum is also shown in Fig. 6 between 0 and 950 cm^{-1}. Above 950 cm^{-1} Saturn's brightness temperature was assumed to be that of a blackbody of 115°K. The contribution of the spectral range above 950 cm^{-1} to the thermal emission is small; the blackbody approximation is therefore adequate.

The spectral integration was carried out in four segments. First, the model spectrum was integrated from 0 to 200 cm^{-1} (6.909 10^{-5} W cm^{-2} sr^{-1}); second, the measured radiance from 200 to 500 cm^{-1} (7.189 10^{-5} W cm^{-2} sr^{-1}) was included; third, the model was integrated again from 500 to 950 cm^{-1} (0.514 10^{-5} W cm^{-2} sr^{-1}); and finally, a blackbody of 115°K was integrated from 950 to 2000 cm^{-1} (0.074 10^{-5} W cm^{-2} sr^{-1}). The value of 6.909 10^{-5} W cm^{-2} sr^{-1} for the low wavenumber integration includes a 1.19% reduction in radiance to account for differences in the limb functions between this spectral interval and the measured interval from 200 to 500 cm^{-1}. Above 500 cm^{-1} no such correction was applied. Sum-

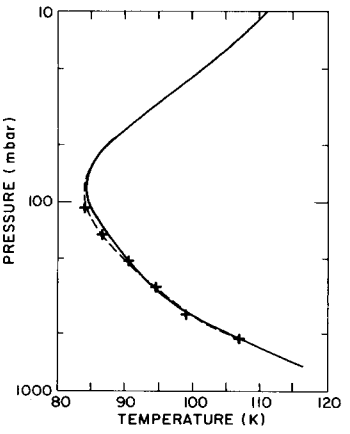

FIG. 7. Temperature profiles derived from the measured full-disk spectrum (solid line) shown in Fig. 6 and from a weighted average of spectra (dashed line) in the north–south mapping sequence.

ming all four spectral segments yields 14.686 10^{-5} W cm^{-2} sr^{-1} or a flux of 4.614 10^{-4} W cm^{-2}; this flux corresponds to an effective temperature of 94.98°K.

7. ENERGY BALANCE

The solar constant at the Earth is 0.1374 W cm^{-2} (Willson *et al.* 1980) and at the mean distance of Saturn (9.552 AU) 1.506 10^{-3} W cm^{-2}. With a Bond albedo of 0.342 the cross section of Saturn (1.0434 10^{20} cm^2, which includes the correction for varying projected area around the orbit due to Saturn's obliquity) would absorb 1.033 10^{17} W. However, this power is reduced by the ring shadows and increased by light scattered by the rings as well as by thermal emission from the rings. The effect of the rings has to be calculated not for the actual time of the measurement, as was the case for the corrections to the measured values, but for the annual or seasonal mean.

To calculate the seasonal mean of the ring shadowing, we use a procedure (Appendix F) similar to that for the ring obscuration (Appendix B), but which allows integration over the orbital position of Saturn for one season. Summing over all rings and adjusting the result, which is calculated for a sphere, to an ellipsoid with the oblateness of Saturn yields an average ring obscuration of 9.11%. Therefore, only 0.9391 10^{17} W of direct sunlight reach Saturn in one season.

The total power absorbed by Saturn must also include solar radiation scattered from the rings (Appendix G). Integration of the ring contribution over the whole sphere of Saturn yields the incident power scattered by the rings. In each season Saturn receives an additional 0.0681 10^{17} W from the Sun via radiation scattered from the rings. The total solar power which Saturn absorbs is therefore 1.0072 10^{17} W.

To obtain an estimate of the radiative flux from the rings toward Saturn the apparent solid angle of the rings was calculated for different latitudes, using the ring parameters discussed previously, and then integrated over a Saturnian hemisphere. The solid angles divided by 2π are 0.0303, 0.1012, and 0.0314 for the A, B, and C rings, respectively (see Appendix H). To estimate the seasonal average of the flux from the rings we use an estimate of the appropriate mean value of the brightness temperature of the individual rings as they face Saturn. The instantaneous thermal emission of the rings must be averaged over season and phase angle. Temperature data from Voyager (Hanel *et al.*, 1981, 1982) and Pioneer (Froidevaux and Ingersoll, 1980) are consistent with the models developed by Froidevaux (1981) for the seasonal variation of thermal flux at low phase angles. Seasonal averaging of these results gives the mean temperatures for the rings (the effect of eclipses of the rings by Saturn is neglected); we take these as representative of the sunward-facing portion of particles on the illuminated side of the rings. The C ring is optically thin, so the temperature on the sunward side of particles on the "unilluminated" side of this ring is taken as the same as that on the illuminated side; the temperatures of the unilluminated side of the A and B rings, and of the antisunward hemisphere of particles in all three rings are taken as 55°K, in accordance with Voyager (Hanel *et al.*, 1981, 1982), Pioneer (Froidevaux and Ingersoll, 1981), and ground-based (Tokunaga *et al.*, 1980) measurements. Assuming that the particle surfaces radiate in accordance with the Lambert law, each hemisphere is weighted equally to account for the phase function; the resulting equivalent annual mean temperatures of the rings as seen from Saturn are then 63, 62, and 84°K for the A, B, and C rings, respectively. With these values, the rings contribute an additional 0.1064 10^{17} W to Saturn. The total solar and infrared power absorbed by Saturn is therefore 1.1136 10^{17} W.

With a surface area of 4.284 10^{20} cm^2 this corresponds to a flux of 2.599 10^{-4} W cm^{-2}. If Saturn had no internal heat source this flux would lead to an equilibrium tempera-

ture of 82.29°K. If Saturn had no rings but the same Bond albedo and no internal heat source, the required equilibrium temperature would be 80.76°K. Thus obscuration and scattering of sunlight and thermal emission by the rings provide a net warming of 1.52°K.

Dividing the total emitted power of 1.977 10^{17} W by the total absorbed power of 1.1136 10^{17} W yields the energy balance of 1.775. The internal heat source is 8.630 10^{16} W, which gives rise to an average internal flux of 2.015 10^{-4} W cm^{-2}. The average internal heat per volume element (volume of Saturn = 8.31485 10^{29} cm^3) is 1.038 10^{-13} W cm^{-3} and that per mass element is 1.518 10^{-13} W g^{-1}, assuming a mean density of 0.6837 g cm^{-3}. With a total solar power of 3.8642 10^{26} W the Saturnian luminosity ratioed to the Sun is $\log L/L_{\text{Sun}} = -9.651$.

8. ERROR ANALYSIS FOR THERMAL EMISSION AND ENERGY BALANCE

The error analysis of the thermal emission measurement is summarized in Table IV. We have taken the standard deviation in the selected spectra (integrated from 200 to 500 cm^{-1}) divided by the integrated radiance as the basis of the error, and assigned an uncertainty of 1.03% to the measurement itself. This error estimate is considerably larger than the noise in the interferometer and also larger than the corresponding quantity at Jupiter (see Paper 1). The larger error reflects the lower Saturn radiances as well as pointing uncertainties. The field-of-view factor is well known, resulting in an estimated error of 1%. The uncertainties in the ring emission and in the term accounting for deviations in the uniformity of the response within the field of view are assumed to be known within 20%, and ring obscuration within 10%. As stated above, the uncertainty in the 200 to 500-cm^{-1} contribution derived from the north–south mapping sequence is taken as 0.010×10^{-4} W cm^{-2} sr^{-1}. The weighted mean of the mapping and disk results therefore has a probable error of 0.008×10^{-4} W cm^{-2} sr^{-1}, this contributes an error of 0.6% to the Saturnian thermal emission, since this portion of the spectrum contributes 49% of the total.

The combined uncertainty due to errors in the derived temperature profile and to the precision of the radiative transfer model was assumed to be 3%; limitations are mostly in the knowledge of the absorption coefficients but the effect of atmospheric haze may also contribute. With 51% of the thermal emission originating from integration of the radiative transfer model, the overall error due to uncertainties in the model is 1.5%. The total error in the full-disk data is 1.6%, which translates into a probable error of 0.4°K in the effective temperature.

The errors in the terms used to calculate the energy balance and internal heat source of Saturn are summarized in Table V. The value of the solar constant at Earth used in our calculations is the same as in Paper 1. The seasonal effect of the ring shadow is estimated to be known within 10% and the scattering of light and the thermal emission by the rings onto Saturn within 20%. The probable error for the total absorbed power is 4.5%.

The energy balance of Saturn and the internal heat are therefore known to within 4.8 and 6.9%, respectively; the effective temperature of Saturn is 95.0 ± 0.4°K.

9. DISCUSSION

The bolometric Bond albedo of Saturn of ~0.34 derived from the Voyager IRIS measurements is considerably lower than the values used by previous investigators, as shown in Table I. Most of the difference is caused by the lower geometric albedo measured by IRIS. Our evaluation of this quantity includes a consistent but somewhat complex analysis of ring effects. This analysis is not the source of the discrepancy, however, since two other determinations of the zero-phase radiometer signal using data less representative of the globe, but involv-

TABLE V

SUMMARY OF ENERGY BALANCE TERMS AND ERRORS

Quantity	Value	Uncertainty	Contributing error (%)
$P = S\Sigma(1 - A_{Sat})(1 - e_1) + e_2 + e_3$			
S: Solar constant at Saturn (10^{-3} W cm^{-2})	1.506	0.008	0.4
Σ: Seasonal average Saturn cross section (10^{20} cm^2)	1.043	—	—
A_{Sat}: Bond albedo	0.342	0.030	3.8
e_1: Seasonal ring shadow effect	0.0911	10%	0.8
e_2: Seasonal ring scattering (10^{17} W)	0.0681	20%	1.2
e_3: Seasonal ring emission (10^{17} W)	0.1064	20%	1.9
P: Total absorbed power (10^{17} W)	1.114	0.050	4.5
Emitted thermal flux (10^{-4} W cm^{-2})	4.614	0.075	1.6
Emitted thermal power (10^{17} W)	1.977	0.032	1.6
Effective temperature (°K)	94.98	0.39	
Internally generated heat (10^{17} W)	0.863	0.060	6.9
Internally generated flux (10^{-4} W cm^{-2})	2.01	0.14	6.9
Energy balance	1.78	0.09	4.8

ing little or no ring correction, are quite consistent with the detailed analysis (Appendix E). Furthermore, the net effect of the rings is only about 10% (see Table III), while the discrepancy is ~50%. Finally, the Voyager analysis of the geometric albedo of Jupiter (Paper 1) agrees well with the careful photometric measurements of Taylor (1965), and the radiometer showed little degradation with time.

With a lower Bond albedo and full consideration of ring effects, the equilibrium temperature that we derive, ~82°K, is higher than previous estimates, which range from ~75 to 78°K.

The effective temperature derived in this analysis, 95.0°K, is generally in accord with previous measurements considering the large uncertainties and difficulties in these measurements from Earth. The energy balance of Saturn, 1.78, derived in this analysis is lower than all previous estimates, except those of Wright (1976) and Ward (1977); however, the results of these authors are fortuitous as a comparison of equilibrium and effective temperatures shows (Table I). As a consequence of the lower energy balance the internal flux derived in this paper, 2.01 10^{-4} W cm^{-2}, is also lower than what most previous authors obtain.

A summary of the spectral information used in determining the energy balance of Saturn is displayed in Fig. 8 in a format similar to that for Jupiter (Fig. 6 of Paper 1). Below 200 cm^{-1} the radiative transfer calculations were used and between 200 and 950 cm^{-1} the average of the eight measured disk spectra is shown. The solar spectrum is adjusted for the mean distance of Saturn and the reflected Saturn spectrum is adjusted to a Bond albedo of 0.34 as indicated by this analysis.

The major parameters which enter the energy balance determination and their probable errors are summarized in Table VI. The Saturn values are from this analysis; the Jupiter values are from Paper 1, with the exception of the internal power per unit mass, which was not explicitly given in Paper 1. Although the geometric albedo of Saturn is lower than that of Jupiter, the Bond albedos of the two planets are nearly the same because of the larger phase integral of Saturn. The energy balance of Saturn is only slightly larger than that of Jupi-

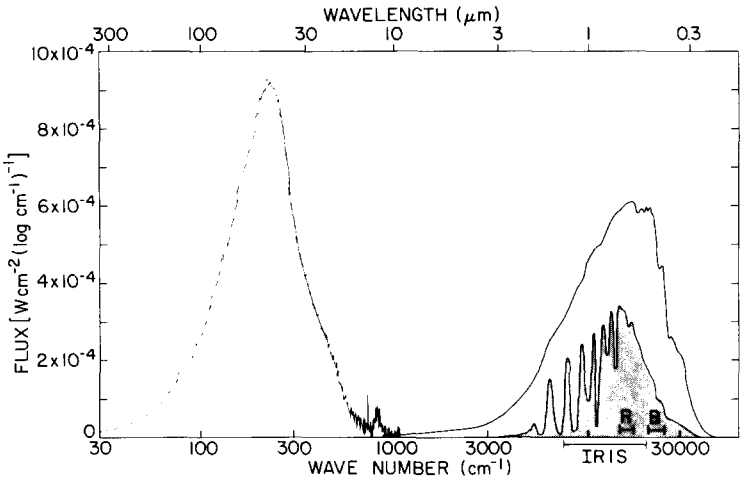

FIG. 8. Summary of spectral information determining the energy balance of Saturn. The thermal emission between 200 and 950 cm^{-1} is from the disk measurement; below that range the emission is from the radiative transfer model. In evaluating the total thermal emission the 500- to 950-cm^{-1} range was also represented by the model. The incident solar spectrum at Saturn is indicated by the upper curve on the right. The reflected solar spectrum (lower curve) was normalized to a Bond albedo of 0.34. The radiometer samples about 72% of this reflected energy. The half-power points of the Pioneer red and blue channels and of the IRIS radiometer are indicated in the vertical bars labelled R, B, and IRIS, respectively.

ter. Since Saturn is less massive than Jupiter, it has less primordial heat and must augment its thermal emission with energy from another source, such as helium differentiation, in order to yield an energy balance comparable to that of Jupiter.

The luminosity of Saturn (log L/L_{Sun} = −9.65) derived in this analysis removes approximately one-third of the discrepancy between observation and model calculations of Grossman *et al.* (1980, see their Fig. 8c). We suspect that the discrepancy will be further reduced for models of the interior of Saturn which include the effect of helium differentiation and which are consistent with the helium depletion of the outer atmospheric regions (Y = 0.13) derived from the Voyager infrared spectra (Conrath *et al.*, 1982).

In the derivation of the energy balance we neglected possible secular changes in Saturn's albedo as well as the effect of Saturn's orbital eccentricity. Five months after the Voyager 1 encounter, Saturn passed the point in its orbit which corresponds to the mean distance from the Sun, $a(1 + \varepsilon^2/2)$ = 9.552 AU, moving toward aphelion (the semimajor axis and eccentricity are a and ε, respectively). The radiative time constant at the level where the atmospheric temperature equals the effective temperature of ~95°K (~300 mbar) is on the order of 30 years, about one orbital period of Sat-

TABLE VI

COMPARISON OF ENERGY BALANCE PARAMETERS FOR JUPITER AND SATURN

Quantity	Jupiter	Saturn
Geometric albedo	0.274 ± 0.013	0.242 ± 0.012
Phase integral	1.25 ± 0.1	1.42 ± 0.1
Bond albedo	0.343 ± 0.032	0.342 ± 0.030
Total absorbed power (10^{17} W)	5.014 ± 0.248	1.114 ± 0.050
Total emitted power (10^{17} W)	8.365 ± 0.084	1.977 ± 0.032
Effective temperature (°K)	124.4 ± 0.3	95.0 ± 0.4
Energy balance	1.67 ± 0.09	1.78 ± 0.09
Internal energy source (10^{17} W)	3.35 ± 0.26	0.863 ± 0.060
Internal energy flux (10^{-4} W cm^{-2})	5.44 ± 0.43	2.01 ± 0.14
Internal power/mass (10^{-13} W g^{-1})	1.76 ± 0.14	1.52 ± 0.11
Luminosity: log(L/L_{Sun})	−9.062 ± 0.034	−9.651 ± 0.030

urn. In contrast, the radiative time constant at Jupiter is only 9 months at the level corresponding to the Jovian effective temperature of 124°K. The change in insolation due to the orbital eccentricity of Saturn is ±10%, but the effect is greatly reduced by the high thermal inertia implied by the long time constant. To first order the effect due to the 10% change in insolation is reduced by a factor of 6 to approximately 1.7%. In this paper we have neglected the effect of the orbital eccentricity and have calculated the energy balance for the orbital distance of Saturn corresponding to the average with respect to time, 9.552 AU.

The Voyager approach asymptote at Saturn was about 8.8° above the ring plane. Therefore, the northern hemisphere contributes slightly more to the disk measurement than does the southern hemisphere. Seasonal differences exist between hemispheres at certain atmospheric levels, but at the pressure level where the bulk of the thermal emission originates, ~300 mbar, the hemispherical differences are small (Hanel *et al.*, 1982) and have been neglected in this analysis.

For some of the requirements of this investigation, such as the calculation of the seasonal effect of the ring shadow, analyses have been performed previously (Brinkman and McGregor, 1979), but for many other effects the required calculations were not available. Here, we use a self-consistent treatment of all ring effects. We believe the limitations in the computations of the ring effects are primarily in uncertainties caused by the parameterization of the optical depth and estimated seasonal mean temperature of the individual rings, and in the knowledge of the phase functions of Saturn and the rings.

APPENDIX A: CALCULATIONS OF THE FRACTION OF RINGS WITHIN THE FIELD OF VIEW BUT OUTSIDE THE DISK OF SATURN

Figure A1 shows one quadrant of the field of view with radius c, the disk of Saturn with equatorial and polar radii a and b,

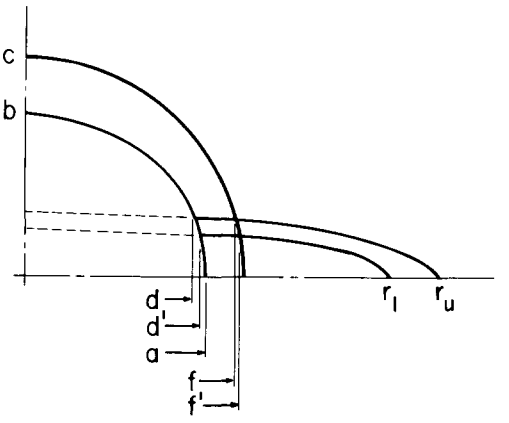

FIGURE A1

and a ring with lower and upper radii, r_l and r_u. The intersections of the elliptical projection of the rings with the Saturn ellipse are d and d', and with the circular field of view f and f', respectively. The abscissae of these intersections are

$$d = a\left(\frac{b^2 - r_u^2 \sin^2\alpha}{b^2 - a^2 \sin^2\alpha}\right)^{1/2},$$

$$d' = a\left(\frac{b^2 - r_l^2 \sin^2\alpha}{b^2 - a^2 \sin^2\alpha}\right)^{1/2},$$

$$f = \frac{(c^2 - r_u^2 \sin^2\alpha)^{1/2}}{\cos\alpha},$$

$$f' = \frac{(c^2 - r_l^2 \sin^2\alpha)^{1/2}}{\cos\alpha}.$$

The subspacecraft latitude and the apparent tilt of the rings, α, was 8.825°. Expressing the radial dimensions in terms of the equatorial radius of Saturn ($R_S = 1$), the polar radius is 0.90399. The individual ring radii, r_u and r_l, are also expressed in R_S. Applying elementary trigonometry, the area of interest can be shown to be

$$A_{\text{ring}} = \frac{2}{c^2}$$
$$[\sin\alpha\, r_u^2(\arcsin f/r_u - \arcsin d/r_u)$$
$$- \sin\alpha\, r_l^2(\arcsin f'/r_l - \arcsin d'/r_l)$$
$$+ c^2(\arcsin f'/c - \arcsin f/c)$$
$$- ab(\arcsin d'/a - \arcsin d/a)].$$

The ring area for all four segments is expressed as a fraction of the circular field of view. For each ring this geometric factor is then multiplied by the apparent opacity factor of the ring $[1 - \exp(-\tau/\sin\alpha)]$, where τ is the normal optical thickness.

APPENDIX B: CALCULATION OF FRACTION OF RING OBSCURATION

The "Shadow 1" program calculates the area normal to the line from the spacecraft to Saturn which intercepts a ring (A, B, or C) and the disk of Saturn, multiplies it by the projected ring opacity, and normalizes the result to the circular cross section of Saturn. For all cases of interest the ring shadow intercepts the Saturn limb at relatively low latitudes, so the spherical Saturn model is an acceptable approximation. The elliptical cross section of Saturn is then accounted for by dividing the result by 0.90399, the ratio of the polar to equatorial diameter of Saturn which is also the ratio of the elliptical to circular cross section for the same equatorial radius. The integration is carried out in the ring plane, integrating over the azimuth, ϕ, in closed form and over the radius, r, numerically using Simpson's rule. The integration limits must be chosen carefully. The limits in r may be the inner or outer ring boundaries or the apparent horizon and in ϕ the boundary determined by the line-of-sight striking the limb or again the horizon of the surface element da_1 on Saturn. Formally the program evaluates the function

$$F(\alpha) = 2\sin\alpha\left[1 - \exp\left(-\frac{\tau}{\sin\alpha}\right)\right]$$

$$\int_{r_l}^{r_u} dr\, r \left\{ -\cos^{-1}\left(\frac{1}{r\sqrt{1 - \sqrt{r^2 - 1}\sin\alpha}}\right) + \frac{1}{\alpha}\left[\frac{\pi}{2} + \alpha - \cos^{-1}(\sqrt{r^2 - 1}\sin\alpha)\right] \cos^{-1}\left(\frac{\frac{\pi}{2}\alpha}{\frac{\pi}{2} + \alpha - \cos^{-1}(\sqrt{r^2 - 1}\sin\alpha)}\right)\right\},$$

where α is the angle between the spacecraft–Saturn line and the ring plane and r is the radius vector expressed in Saturn radii.

APPENDIX C: CALCULATION OF LIGHT REFLECTED FROM RINGS ONTO THE DISK OF SATURN

The program calculates the sunlight reflected from the illuminated side of the rings onto a small area element, da_1, on Saturn. Saturn is assumed to be spherical; since most of the energy is deposited at low latitudes, this approximation is acceptable.

The energy falling on the area element da_1 located at Saturn's azimuth ϕ ($\phi = 0$ is the subsolar meridian), colatitude θ, and Saturn's orbital position S may be expressed by

$$\frac{dW(\phi, \theta, S)}{da_1} = \int_{r_l}^{r_u} dr \int_{\phi'_{\min}}^{\phi'_{\max}} d\phi'\, r\sin\alpha\cos\theta\, F(\psi) \cdot \frac{\left[1 - \exp\left(-\tau\sqrt{1 + r^2 - 2r\sin\theta\cos(\phi - \phi')}\right)\right][r\sin\theta\cos(\phi - \phi') - 1]}{\cos\theta\,\{[1 + r^2 - 2r\sin\theta\cos(\phi - \phi')]^2}.$$

The lower and upper integration limits for r and ϕ' are r_l, r_u, $\phi'_{\min}$, and $\phi'_{\max}$, respectively. They must be chosen carefully. The first condition for the limits requires the ring element, da_2, to be visible from the element on Saturn, da_1. The second condition requires the ring element to be illuminated by the Sun; the shadow boundary must therefore be established. On the dark region of Saturn, near the antisolar longi-

tude, two illuminated ring segments may be visible from da_1. The angle α is related to the angular position of Saturn with respect to the Sun by

$$\alpha = \alpha_{\max} \sin S,$$

where $\alpha_{\max}$ is Saturn's obliquity, 26.745°.

$F(\psi)$ is the phase function of the ring area da_2 as a function of ψ, which is the angle defined by the lines between the Sun, da_2 and da_1. The phase function assumed in these calculations is that of a Lambert sphere augmented by reflected light from Saturn, also assumed to scatter in a Lambertian fashion. This function was then approximated by a series in terms of cos ψ:

$$F(\psi) = 0.334 + 0.41 \cos\psi + 0.257 \cos^2\psi + 0.065 \cos^3\psi - 0.066 \cos^4\psi.$$

After computing a value for every 10° in latitude and longitude (for S corresponding to the time of measurement), integration over the apparent disk was carried out using appropriate weighting functions. The calculations were carried out for each ring separately.

APPENDIX D: CALCULATION OF RESTRICTED PHASE FUNCTION FOR MINNAERT ELLIPSOID

Consider Saturn to be a Minnaert ellipsoid with equatorial and polar radii a and b, respectively, i.e., an ellipsoid with surface scattering governed by

$$I\mu = I_0(\mu\mu_0)^k,$$

where I is the observed radiance from unit area, I_0 is the radiance under conditions of normal illumination and viewing, and μ and μ_0 are the cosines of the illumination and observation angles, respectively, measured from the surface normal. For the restricted case when the Sun and the observer are in the equatorial plane (approximating conditions for the Voyager observations) the double integral for the phase function is separable, leading to

$$\Pi\left(\phi_0, \frac{a}{b}, k\right) = I_0 \frac{\Gamma(k+1)}{2\sqrt{\pi}\,\Gamma\left(\frac{2k+3}{2}\right)} \int_{\phi_0 - \frac{\pi}{2}}^{\frac{\pi}{2}} d\phi \cos^k\phi \cos^k(\phi - \phi_0) \cdot \frac{a}{b} \frac{2\Gamma\left(\frac{2k+3}{2}\right)}{\sqrt{\pi}\,\Gamma(k+1)} \int_0^{\pi} d\theta \frac{\sin^{2k+1}\theta}{\left(\sin^2\theta + \frac{a^2}{b^2}\cos^2\theta\right)^2 \left(\sin^2\theta + \frac{a^4}{b^4}\cos^2\theta\right)^{k-\frac{1}{2}}}$$

$$= \Phi(\phi_0, k) \cdot F\left(\frac{a}{b}, k\right),$$

where Π, θ, ϕ, and ϕ_0 are disk radiance, colatitude, azimuth, and phase angle, respectively; in addition, Φ is the phase function of a Minnaert sphere, F is a shape factor which accounts for planetary ellipticity, and Γ is the gamma function.

From a phase angle of 12.65°, the correction to zero phase is a factor of 1/0.97724. For Saturn, a = 60330 km, b = 54538 km, and the ellipticity correction is $F(1.10620, 0.9)$ = 1.01128.

APPENDIX E: INTERNAL CONSISTENCY OF DISK AND SPATIALLY RESOLVED RADIOMETER MEASUREMENTS

By using full-disk observations and the limb darkening parameter, k, determined from high-resolution data, a value of 221.7 DN was obtained for the full-disk radiometer signal of Saturn at zero phase in the absence of rings. If the Minnaert representation, with constant k and I_0, is assumed to be valid over the disk at low phase angles,

then two straightforward methods employing high-resolution data alone provide the same quantity.

In addition to determining k, the fit to the data of Fig. 4 also yields I_0 = 304.1 DN. This brightness for normal viewing of the subsolar point can be converted to a zero-phase disk brightness by integrating the Minnaert function over the illuminated hemisphere to give

$$\frac{2I_0}{2k + 1} = 217.2 \text{ DN}.$$

The ellipticity of Saturn increases this by a factor of 1.011 (Appendix D). Combining this with the degradation correction gives a disk signal of 219.7 DN.

A related approach can be used if the subsolar point brightness is measured directly. Sequences of east–west and north–south scans recorded at approximately 60 and 36 hr before closest approach show maxima in the radiometer channel of 337 and 338 DN, respectively. For these observations the footprint diameters were 0.131 and 0.069 of the disk diameter, while the emission angles at the subsolar point were 14.7 and 17.0°. From the calculations of Appendix C, 2% of the light reflected from Saturn at zero phase and +10° latitude results from illumination by scattered ring light, assuming that the reflectivity of the rings is 0.6 and that of the planet is 0.34. The radiometer readings are therefore reduced by 6.9 DN. Integrating the Minnaert function over the IRIS footprint and correcting to normal viewing gives values of I_0 equal to 330.1 and 329.9 DN, respectively, for an average of 330.0 DN. Multiplying by $2/(2k + 1)$ and correcting for planetary ellipticity and instrument degradation, we obtain a full-disk brightness (in the absence of rings) of 239.3 DN.

The differences between the zero-phase full-disk signals based on disk measurements (221.7 DN), on the limb function in the southern hemisphere (219.7 DN), and on subsolar point observations (239.3 DN) are primarily due to real contrast on Saturn. The 10% difference between the IRIS broadband, high spatial resolution results appears to be quite consistent with the contrasts at orange or blue visual wavelengths shown in Fig. 6 of Smith *et al.* (1981). In addition, the value derived from the disk measurements falls between the other determinations, as the figure suggests might be the case. Thus three rather different determinations of the disk signal are in harmony with one another, lending confidence to the geometric albedo we derive.

APPENDIX F: CALCULATION OF THE SEASONAL MEAN SHADOW EFFECT OF THE RINGS ON SATURN

This program, Shadow 2, is similar to the Shadow 1 program discussed in Appendix B. However, instead of calculating the shadow effect for one point in the Saturn season, i.e., for one value of S, the Shadow 2 program integrates over one full season (S = 0 to 90°). Steps in S are 10°. Again, summation over rings A, B, and C is required.

APPENDIX G: SCATTERED LIGHT FROM RINGS EVALUATED FOR ONE SEASON

The calculation for the seasonal mean effect of scattered sunlight from the rings uses the same basic program as described in Appendix C. However, the calculations are carried out for every 15° in S, instead of for S = 8.3136°, which is the value of S at the time of observation. The integrations are carried out over the sphere first, then θ, and finally over S from 0 to 90°. Results from all three rings are then summed.

APPENDIX H: CALCULATION OF THERMAL EMISSION FROM RINGS ONTO SATURN

The thermal emission from each ring is calculated by weighting the thermal radiance by the integral

$$\frac{d\bar{\Omega}}{d\theta} = 4\pi \sin\theta \cos\theta \int_{r_1}^{r_2} dr \int_0^{\cos^{-1}\left(\frac{1}{r\cos\theta}\right)} d\phi \left[1 - \exp\left(-\frac{\tau\sqrt{1 + r^2 - 2r\sin\theta\cos\phi}}{\cos\theta}\right)\right] \cdot \frac{r\sin\theta\cos\phi - 1}{[1 + r^2 - 2r\sin\theta\cos\phi]^2}.$$

The terms r, θ, and ϕ have the same meaning as before: radius from the center of Saturn, colatitude, and azimuth, respectively. The function $d\bar{\Omega}/d\theta$ is then integrated numerically over θ for each ring.

ACKNOWLEDGMENTS

We thank Dr. M. Tomasko for providing the Saturnian phase integral at red and blue wavelengths. We also thank Drs. D. P. Cruikshank and J. Hardorp for making Saturn spectra available, and Drs. D. Gautier and A. Ingersoll for helpful discussions. Mr. L. Mayo and J. Frost of Automation Horizons Inc. provided technical assistance in the data analysis. Ms. L. Herada helped in the numerical computations.

Note added in proof. The last line of Table II, and the drop in radiometer sensitivity at Saturn (Figure 1) are slightly in error; the post Saturn calibration measurement was made on January 9, rather than January 13, 1981. None of the results of this paper are affected, however, since all observations used here were obtained prior to the actual encounter.

REFERENCES

AUMANN, H. H., C. M. GILLESPIE, JR., AND F. J. LOW (1969). The internal powers and effective temperatures of Jupiter and Saturn. *Astrophys. J.* **157,** L69–L72.

BINDER, A. B., AND D. W. MCCARTHY, JR. (1973). IR spectrophotometry of Jupiter and Saturn. *Astron. J.* **78,** 939–950.

BRINKMAN, A. W., AND J. MCGREGOR (1979). The effect of the ring system on the solar radiation reaching the top of Saturn's atmosphere: Direct radiation. *Icarus* **38,** 479–482.

CAMERON, A. G., AND J. B. POLLACK (1976). On the origin of the solar system and of Jupiter and its satellites. In *Jupiter* (T. Gehrels, Ed.), pp. 61–84. Univ. of Arizona Press, Tucson.

CONRATH, B. J., D. GAUTIER, R. A. HANEL, AND J. HORNSTEIN (1982). The helium abundance on Saturn obtained from Voyager 1 infrared measurements. Paper presented at Saturn Conference, Tucson, Arizona, May 1982.

COURTIN, R., P. LÉNA, M. DE MUIZON, D. ROUAN, C. NICOLLIER, AND J. WIJNBERGEN (1979). Far infrared photometry of planets: Saturn and Venus. *Icarus* **38,** 411–419.

COURTIN, R., D. GAUTIER, A. MARTEN, AND W. MAGUIRE (1981). The acetylene and ethane abundances and the phosphine distribution in Saturn's atmosphere from the Voyager 1–IRIS experiment. *BAAS* **13,** 722.

CRUIKSHANK, D., AND J. HARDORP (1981). Private communication.

CUZZI, J. (1978). The rings of Saturn: State of current knowledge and some suggestions for future studies. In NASA conference publication 2068. D. Hunten and D. Morrison editors.

ERICKSON, E. F., D. GOORVITCH, J. P. SIMPSON, AND D. W. STRECKER (1978). Far infrared spectrophotometry of Jupiter and Saturn. *Icarus* **35,** 61–73.

FINK, U., AND H. P. LARSON (1979). The infrared spectra of Uranus, Neptune, and Titan from 0.8 to 2.5 microns. *Astrophys. J.* **233,** 1021–1040.

FLASAR, F. M. (1973). Gravitational energy sources in Jupiter. *Astrophys. J.* **186,** 1097–1106.

FROIDEVAUX, L. (1981). Saturn's rings: Infrared brightness variation with solar elevation. *Icarus* **46,** 4–17.

FROIDEVAUX, L., AND A. P. INGERSOLL (1980). Temperatures and optical depths of Saturn's rings and a brightness temperature for Titan. *J. Geophys. Res.* **85,** 5929–5936.

GAUTIER, D., AND R. COURTIN (1979). Thermal profiles of giant planets. *Icarus* **39,** 28–45.

GAUTIER, D., B. CONRATH, M. FLASAR, R. HANEL, V. KUNDE, A. CHEDIN, AND N. SCOTT (1981). The helium abundance on Jupiter from Voyager. *J. Geophys. Res.* **86,** 8713–8720.

GRABOSKE, H. C., JR., J. B. POLLACK, A. S. GROSSMAN, AND R. J. OLNESS (1975). The structure and evolution of Jupiter, the fluid contraction phase. *Astrophys. J.* **199,** 265–281.

GROSSMAN, A. S., J. B. POLLACK, R. T. REYNOLDS, AND A. L. SUMMERS (1980). The effect of dense cores on the structure and evolution of Jupiter and Saturn. *Icarus* **42,** 358–379.

HANEL, R., D. CROSBY, L. HERATH, D. VANOUS, D. COLLINS, H. CRESWICK, C. HARRIS, AND M. RHODES (1980). Infrared spectrometer for Voyager. *Appl. Opt.* **19,** 1391–1400.

HANEL, R. A., B. J. CONRATH, L. W. HERATH, V. G. KUNDE, AND J. A. PIRRAGLIA (1981a). Albedo, internal heat, and energy balance of Jupiter: Preliminary results of the Voyager infrared investigation. *J. Geophys. Res.* **86,** 8705–8712.

HANEL, R., B. CONRATH, F. M. FLASAR, V. KUNDE, W. MAGUIRE, J. PEARL, J. PIRRAGLIA, R. SAMUELSON, L. HERATH, M. ALLISON, D. CRUICKSHANK, D. GAUTIER, P. GIERASCH, L. HORN, R. KOPPANY, AND C. PONNAMPERUMA (1981b). Infrared observations of the Saturnian system from Voyager 1. *Science* **212,** 192–200.

HANEL, R., B. CONRATH, F. M. FLASAR, V. KUNDE, W. MAGUIRE, J. PEARL, J. PIRRAGLIA, R. SAMUELSON, D. CRUICKSHANK, D. GAUTIER, P. GIERASCH, L. HORN, AND C. PONNAMPERUMA (1982). Infrared observations of the Saturnian system from Voyager 2. *Science* **215,** 544–548.

HUBBARD, W. B. (1968). Thermal structure of Jupiter. *Astrophys. J.* **152,** 745–754.

HUBBARD, W. B. (1973). Observational constraint on the structure of hydrogen planets. *Astrophys. J.* **182,** L35–L38.

HUBBARD, W. B. (1980). Intrinsic luminosities of the Jovian planets. *Rev. Geophys. Space Phys.* **18**(1), 1–9.

HUBBARD, W. B. (1981). Interiors of the giant planets. *Science* **214,** 145–149.

HUBBARD, W. B., AND R. SMOLUCHOWSKI (1973). Structure of Jupiter and Saturn. *Space Sci. Rev.* **14,** 599–662.

IRVINE, W. M., AND A. P. LANE (1971). Monochromatic albedos for the disk of Saturn. *Icarus* **15,** 18–26.

KLIORE, A. J., I. R. PATEL, G. F. LINDAL, D. N. SWEETNAM, AND H. B. HOTZ (1980). Structure of the ionosphere and atmosphere from Pioneer 11 Saturn radio occultation. *J. Geophys. Res.* **85,** 5857–5870.

LAMBERT, D. (1978). The abundances of the elements in the solar photosphere. VIII. Revised abundances of carbon, nitrogen and oxygen. *Mon. Not. Roy. Astron. Soc.* **82,** 249–272.

LOW, F. J. (1965). Planetary radiation at infrared and millimeter wavelengths. *Lowell Obs. Bull.* **128**(9), 184–187.

MENZEL, D. H., W. W. COBLENTZ, AND C. O. LAMPLAND (1926). Planetary temperatures derived from watercell transmissions. *Astrophys. J.* **63,** 177–187.

MELNICK, G., R. W. RUSSELL, T. R. GROSNELL, AND M. HARWIT (1982). Private communication.

NOLT, I. G., J. V. RADOSTITZ, R. J. DONNELLY, R. E. MURPHY, AND H. C. FORD (1974). Thermal emission of Saturn's rings and disc at 35 μm. *Nature* **248,** 659–660.

ORTON, G. S., AND A. P. INGERSOLL (1980). Saturn's atmospheric temperature structure and heat budget. *J. Geophys. Res.* **85,** 5871–5881.

POLLACK, J., A. S. GROSSMAN, R. MOORE, AND H. C. GRABOSKE (1977). A calculation of Saturn's contraction history. *Icarus* **30,** 111–128.

RIEKE, G. H. (1975). The thermal radiation of Saturn and its rings. *Icarus* **26,** 37–44.

SALPETER, E. (1973). On convection and gravitational layering in Jupiter and stars of low mass. *Astrophys. J.* **181,** L83–L86.

SMITH, B. A., L. SODERBLOM, R. BEEBE, J. BOYCE, G. BRIGGS, A. BUNKER, S. A. COLLINS, C. J. HANSEN, T. V. JOHNSON, J. L. MITCHELL, R. J. TERRILE, M. CARR, A. F. COOK, II, J. CUZZI, J. B. POLLACK, G. E. DANIELSON, A. INGERSOLL, M. E. DAVIES, G. E. HUNT, H. MASURSKY, E. SHOEMAKER, D. MORRISON, T. OWEN, C. SAGAN, J. VEVERKA, R. STROM, AND V. E. SOUMI (1981). Encounter with Saturn: Voyager 1 imaging science results. *Science* **212,** 163–191.

SMOLUCHOWSKI, R. (1967). Internal structure and energy emission of Jupiter. *Nature* **215,** 691–695.

STEVENSON, D. J. (1980). Saturn's luminosity and magnetism. *Science* **208,** 746–748.

STEVENSON, D. J., AND E. E. SALPETER (1976). Interior models of Jupiter. In *Jupiter* (T. Gehrels, Ed.), pp. 85–112. Univ. of Arizona Press, Tucson.

STEVENSON, D. J., AND E. E. SALPETER (1977). The dynamics and helium distributions in hydrogen–helium planets. *Astrophys. J. Suppl.* **35,** 239–261.

TAYLOR, D. J. (1965). Spectrophotometry of Jupiter's 3400–10000 Å spectrum and a bolometric albedo for Jupiter. *Icarus* **4,** 362–373.

TOKUNAGA, A. T., J. CALDWELL, AND I. G. NOLT (1980). The 20 μm brightness temperature of the unilluminated side of Saturn's rings. *Nature* **287,** 212–214.

TOMASKO, M. G., R. A. WEST, AND N. D. CASTILLO (1978). Photometry and polarimetry of Jupiter at large phase angles. *Icarus* **33,** 558–592.

TOMASKO, M. G., R. S. MCMILLAN, L. R. DOOSE, N. D. CASTILLO, AND J. P. DILLEY (1980). Photometry of Saturn at large phase angles. *J. Geophys. Res.* **85,** 5891–5903.

WALKER, R. G. (1966). *Infrared Photometry of Stars and Planets.* Ph.D. thesis, Harvard University.

WARD, D. B. (1977). Far infrared spectral observations of Saturn and its rings. *Icarus* **32,** 437–442.

WILLSON, R. C., C. H. DUNCAN, AND J. GEIST (1980). Direct measurement of solar luminosity variation. *Science* **207,** 177–179.

WRIGHT, E. L. (1976). Recalibration of the far infrared brightness temperatures of the planets. *Astrophys. J.* **210,** 250–253.